Projet ANR 17-CE22-0002-01
EVNATURB
Programme JCJC 2017

Livrable 1.2: Analysis of heat flux spatio-temporal variability

Leydy Alejandra CASTELLANOS DIAZ (HM&Co-ENPC)

Pierre-Antoine VERSINI (HM&Co-ENPC)

Ioulia TCHIGUIRINSKAIA (HM&Co-ENPC)

Juin 2022

Table of content

RESUME DE LA DEMARCHE 3

SUMMARY 3

1. Statistics of turbulence 4

1.1 Reynolds' decomposition 4

1.2 Statistical moments 4

1.3 Structure function 5

1.4 Fourier Analysis 5

2. Scaling invariance laws for describing fluxes 6

3. Self-similarity extension: from fractal sets to multifractals 8

3.1 Statistical properties of multifractal fields 8

3.2 Legendre Transform 9

3.3 Universal Multifractals (UM) 9

3.4 Trace Moments (TM) 10

3.5 Double Trace Moments (DTM) 11

4. Scaling invariance behaviour of the BGW's thermal fluxes 12

4.1 Data set 12

4.2 Spectral analysis 15

4.3 Structure function scaling exponent 17

5. Characterisation of the scale invariance properties 20

6. Conclusions and Perspectives 25

7. References 27

Résumé de la démarche

L'objet de ce livrable est de présenter les bases méthodologiques et les outils utilisés pour conduire une analyse multi-échelle d'un flux géophysique : géométrie fractale, statistique de la turbulence et analyse multi-fractale. Ces outils ont été mis en œuvre sur les données scintillométriques (C_n^2) et de température collectées en continu pendant 5 semaines sur le campus de l'ENPC. Ce livrable a été réalisé sur la base des travaux de thèse d'Alejandra Castellanos-Diaz.

L'analyse spectrale a montré une invariance d'échelle des deux flux sur une large gamme d'échelle. Les fonctions structures, quant à elles, ont démontré que ces deux séries temporelles sont affectées par un phénomène d'intermittence et qu'elles sont multi-fractales. L'analyse multi-fractale qui en résulte a montré que le C_n^2 est fortement affecté par les fluctuations de température, mais que d'autres champs géophysiques interviennent dans la genèse du flux de chaleur sensible. Ce qui reste à étudier.

Par conséquent, la variabilité spatio-temporelle des flux thermiques sur la Vague Bleue Verte nécessite une analyse plus approfondie, nécessitant davantage de données géophysiques, telles que la vitesse du vent. Cela permettrait de mieux caractériser l'invariance d'échelle ainsi que les propriétés statistiques présentées dans ce travail.

Summary

The purpose of this deliverable is to present the methodological bases and the tools used to conduct a multi-scale analysis of a geophysical flow: fractal geometry, turbulence statistics and multi-fractal analysis. These tools were carried out on scintillometric (C_n^2) and temperature data collected continuously for 5 weeks on the ENPC campus. This deliverable was produced on the basis of the thesis work of Alejandra Castellanos-Diaz.

Spectral analysis showed scale invariance of the two fluxes over a wide range of scales. The structure functions, for their part, demonstrated that these two time series are affected by intermittency and that they are multi-fractal. The resulting multi-fractal analysis showed that C_n^2 is strongly affected by temperature fluctuations, but that other geophysical fields are involved in the genesis of the sensible heat flux. What remains to be studied.

Therefore, the temporal and spatial variability of thermal fluxes in the BGW requires a further analysis with more geophysical data, such as wind speed. This would allow to better characterise the scaling invariance as well as the statistical properties presented in this work.

1. Statistics of turbulence

In complement of the fractal geometry presented in Deliverable 4.2, here are introduced the basic statistics of turbulence. Based on space and time changes of convective and mechanical turbulence, the eddies observed in a variety of turbulent atmospheric fluxes have different sizes and lifetime. This leads to atmospheric fluxes appear stochastic with structure with structure at all scales, and its behaviour difficult to predict. In fact, the chaotic nature of atmospheric turbulence is governed by the non-linearity of Navier-Stokes's equations, for which no formal analytical solution has been found.

The scientific community has been interested by this issue for years and has proposed statistical methods as an appropriate approach to describe turbulence. In this way, statistical properties such as the Reynolds decomposition, the statistical moments, the structure function, and the Fourier series are used to characterise turbulent fluxes. These statistical properties are quite useful for the analysis of spatial and temporal variability of an atmospheric variable observed at some fixed point over long periods, as well as the underlying physical processes. The spatial approach of the structure function will serve in this section to derive the structure function parameter of a scalar, which is the basis for scintillometry technique; while the temporal approach of the structure function will be used in Section 4 to analyse the statistical properties and the scaling behaviour of thermal fluxes measured at a fixed point.

1.1 Reynolds' decomposition

A random atmospheric variable u can be generally described into two parts: the mean $\langle u \rangle$ and the fluctuating about the mean u', as follows:

$$u = \langle u \rangle + u' \qquad (1)$$

The mean of turbulent fluctuations is zero ($\langle u' \rangle = 0$). This decomposition is applied for every turbulent flux in the atmosphere.

1.2 Statistical moments

The random variable u at any position (r) of a four-dimensional space (time or space), can be described with the statistical additive moments $B_{uu\ldots u}$ (Moene et al., 2004). The m-th order moments were defined by Monin & Yaglom (1971), as the mean values of products of m values of the field:

$$B_{uu\ldots u}(r_1, r_2, \ldots, r_m) = \langle u'(r_1)u'(r_2) \ldots u'(r_m) \rangle \qquad (2)$$

where $uu \ldots u$ are integers of which the sum gives the order of the moment. Following the Reynolds' decomposition of the variable u:

$$B_{uu\ldots u}(r_1, r_2, \ldots, r_m) = \langle (u(r_1) - \langle u(r_1) \rangle)(u(r_2) - \langle u(r_2) \rangle) \ldots (u(r_m) - \langle u(r_m) \rangle) \rangle \qquad (3)$$

The first central moment is zero when defined the probability distribution with reference to the mean, and the second central moment is the variance. The general second order moment corresponds to the covariance (B_{uu}) and it is generally used to define three cases of a field (Kesteren, 2012): stationary, homogeneous and isotropic turbulence (Monin & Yaglom, 1971):

- For a *stationary turbulent field*, the mean value $\langle u(t) \rangle$ is constant and invariant under a translation in time $\tau = t_1 - t_2$. Thus, the covariance B_{uu} does not depend on t_1 and t_2:

$$B_{uu}(t_1, t_2) = B_{uu}(t_1 - t_2) \qquad (4)$$

- For a *homogeneous turbulent field*, the mean value $\langle u(r_m)\rangle$ is constant and invariant under a spatial translation. B_{uu} only depends on $r_1 - r_2$:

$$B_{uu}(r_1, r_2) = B_u(r_1 - r_2) \quad (5)$$

- For the *isotropic turbulent field*, the mean value $\langle u(r_m)\rangle$ is constant in all directions and B_{uu} only depends on the distance between two points $r = |r_1 - r_2|$ and not on its direction or position:

$$B_{uu}(r_1, r_2) = B_{uu}(|r_1 - r_2|) = B_{uu}(r) \quad (6)$$

1.3 Structure function

Since atmospheric fields are hardly stationary when the time interval between two measurements is too large (the mean value $\langle u(t)\rangle$ is not constant), Kolmogorov introduced in 1941 the principle of stationary increments. He argued the use of the difference $\Delta u(\tau) = u(t+\tau) - u(t)$ is more practical than $\langle u(t)\rangle$. Then, the second order moment of $\Delta u(\tau)$ (Eq.7) becomes:

$$B_{uu}(t_1, t_2) = \langle \Delta u(t_1) \Delta u(t_2)\rangle \quad (7)$$

$$B_{uu}(\tau) = \langle \big(u(t_1+\tau) - u(t_1)\big)\big(u(t_2+\tau) - u(t_2)\big)\rangle \quad (8)$$

Thus, statistical moments applied to increments of a stochastic process are called structure function. Then, as $B_{uu}(t_1, t_2)$ only depends on the time interval τ, the structure function, between t_1 and t_2, can be introduced as the mean of the difference of the variations of the flux between t_1 and t_2 (Tatarski et al., 1961), as follows:

$$S_{uu}(\tau) = \langle (u(t+\tau) - u(t))^2\rangle \quad (9)$$

In conditions of stationary increments, the second order moment or covariance B_{uu} is related to the second order structure function S_{uu} by:

$$S_{uu}(\tau) = 2(B_{uu}(0) - B_{uu}(\tau)) \quad (10)$$

where, $B_{uu}(0)$ and $B_{uu}(\tau)$ correspond to the statistical moments at any time and at the time interval τ, respectively.

Apart from stationary increments, the principles of locally homogeneous and isotropic fields, for analysing the spatial evolution of the flux between two points of the space can be assumed too. Then, the structure function can be expressed as:

$$S_{uu}(r) = \langle (u(r_1 + r) - u(r_1))^2\rangle \quad (11)$$

In this way, the structure function is a statistical property than only depends on the distance r.

1.4 Fourier Analysis

The Fourier analysis is a widely known method used to decompose the time-domain series of turbulence, into trigonometric functions such as sines and cosines. Hence, the Fourier series of a periodic function $S(t)$ can be expressed as:

$$S(t) = a_0 + \sum_{n=1}^{\infty} a_n \cos(2\pi n f_0 t) + \sum_{n=1}^{\infty} b_n \sin(2\pi n f_0 t) \quad (12)$$

where, f_0 is the fundamental frequency ($1/T$), and a_0, a_n and b_n, the corresponding Fourier coefficients.

Because of the periodicity of events in nature, the Fourier analysis is used with the object to study these amplitudes, frequencies and cycles present on the signal of the turbulent field, as well as its noise. For this purpose, the Fourier transform is used to express a non-periodic function in time $y(t)$ as a continuous series of harmonics, as follows:

$$y(t) = \int_{-\infty}^{+\infty} Y(f)\, e^{2\pi j f t} df \quad (13)$$

where, j is the imaginary unit, f is the frequency, and $Y(f)$ corresponds to the Fourier transform of $y(t)$. Hence, $Y(f)$ converts the signal $y(t)$ to its transform:

$$Y(f) = \int_{-\infty}^{+\infty} y(t)\, e^{-2\pi jft} dt \qquad (14)$$

Let's now consider a discrete version of the Fourier transform known as Discrete Fourier Transform (DTF), where the time series $y(t)$ is measured at just a finite number of times B. So, the DTF results from evaluating the integral from 0 to time T over which the signal is measured:

$$Y(f_b) = \sum_{b=0}^{B-1} y_k\, e^{-2\pi jk_b/B} \qquad (15)$$

where, b is the index of the data array of length B, and k_b the harmonic number. The inverse transform is given by:

$$y(t) = \frac{1}{B}\sum_{b=0}^{B-1} Y(f_b)\, e^{2\pi jk_b/B} \qquad (16)$$

The applicability of DFT was globally extended because of its usability and the development of the Fast Fourier Transform (FFT) algorithm, for which the DFT has been factored and restructured to take advantage of the binary computation processes of the digital computer (Stull, 1988).

Based on the Fourier transform, the power spectral density (or energy spectrum) enables to examine the energy distribution of a turbulent time series data over the frequencies:

$$E(f) = |Y(f)|^2 \qquad (17)$$

The FFT algorithm is usually used to compute $Y(f)$. It is important to note that the FFT is restricted to data sizes 2^b, where $b \leq log_2 S$ and S is the sample size.

The spectral analysis is an approach used to verify the scale invariant properties of a field. In the case of a scaling field, the power spectral density $E(f)$ has a power law relationship with a range of frequency f (temporal analysis) or wave number k (spatial analysis) as:

$$E(f) \sim f^{-\beta} \qquad (18)$$

When this relationship is represented in a log-log scale, the spectral exponent β is deduced from the (absolute) spectral slope.

2. Scaling invariance laws for describing fluxes

In the previous section, fractals were introduced as self-similar complex patterns across different scales, which follows a power law and are characterised by the fractal dimension D_f. Fractals have not only been useful in the study of scaling laws of urban morphology, but also in the analysis of scaling properties of dynamic and non-linear geophysical fields.

Geophysical fields usually exhibit fluctuations that follow scaling power laws. Hence, they were reduced to a fractal set. However, it was found they did not have a unique scaling exponent. When different thresholds (singularities) were set to estimate the distribution pattern of a field, for each singularity a different fractal dimension appeared. This led to define multifractals and their properties, which serves for the analysis and modelling of fields.

Since the measure of a field is generally conducted at a unique scale, the properties at other scales must necessarily be deduced from the measurement scale. Thus, a time series can be

decomposed into frequencies (or wavenumber, by involving the Taylor's hypothesis[1]), in order to analyse the distribution of energy, and the scale invariance of the atmospheric flux can be detected though the spectral exponent β.

To better understand the statistical properties of the fluxes, let's see now a power law that serves for the generalisation of the structure function of an arbitrary moment q at any point x (i.e., integer and non-integer moments q, apart than 2), for analysing of scaling multiplicative processes. Thus, it can be written as:

$$S_a(r) = \langle |\Delta u(r)|^q \rangle$$

$$S_a(r) = \langle |u(x+r) - u(x)|^q \rangle \tag{19}$$

Under the hypothesis of constant energy flux density $\bar{\epsilon}$ and self-similar turbulent flux at small scales, the structure function follows a power law $\zeta(q) = q/3$ as follows:

$$S_a(r) = \bar{\epsilon}^{q/3} r^{q/3}$$

$$S_a(r) = (\bar{\epsilon} r)^{\zeta(q)} \tag{20}$$

where, $\zeta(q)$ is the scaling moment function, related to the similarity exponent $H = 1/3$ by the Kolmogorov theory. In the absence of corrections because turbulent intermittency of the flux, there is a perfect linear relation $\zeta(q) = qH$. Then, for any order moments q:

$$q = 1 \rightarrow \zeta(1) = H$$

$$q = 2 \rightarrow \zeta(2) = 2H \tag{21}$$

$$q = 3 \rightarrow \zeta(3) = 3H$$

For $q = 2$, the second-order moment structure function $\zeta(2)$ is related to the scaling exponent of the spectral analysis β in the following manner:

$$\zeta(2) = \beta - 1$$

$$\beta = 1 + 2H \tag{22}$$

The intermittency is responsible of the extreme variability of the turbulent fluxes in the PBL. Hence, for models considering intermittency, there may be a variation of $\zeta(2) = 2/3$, hence the spectral exponent β is greater than 5/3.

The intermittency could be characterised by the fully knowledge of $\zeta(q)$ and q. The relationship between S_a and r on logarithmic scale, allows to deduce the scaling exponent $\zeta(q)$ as the slope of the linear regression. Hence, the characterization of $\zeta(q)$ over different moments order q enables to determinate the scaling behaviour of the flux (Calif & Schmitt, 2014). Mono-scaling (or monofractal) processes are described by a perfect linear relation $\zeta(q) = qH$. By contrast, the $\zeta(q)$ deviation of the linear trend indicates intermittent multifractal fluctuations, where $\zeta(q)$ is no longer linear, but concave.

Despite K41 demonstrated its utility under homogeneous and isotropic turbulence conditions, some works have shown the limits of these scaling laws. The intermittency of turbulent fluxes is characteristic of strong fluctuations at all scales. Hence, the mean value energy dissipation rate is not constant and insufficient to characterize the turbulence.

This variability motivated Kolmogorov and Obukhov (Kolmogorov, 1962; Obukhov, 1962) to purpose a new theory that considers the intermittency of nonlinear dynamical systems. This

[1] The Taylor's hypothesis of frozen turbulence states that temporal and spatial fluctuations of a flux can be related by a constant velocity. If the turbulence intensity u' is small compared to the mean flux speed $\langle u \rangle$, the temporal response at a fixed point in space can be view as the result of a spatial pattern advected by the mean velocity $\langle u \rangle$.

theory known as K62 considers the structure function of velocity increments is a function of locally averaged energy flux density over a volume of linear dimension r (ϵ_r). In addition, the energy dissipation rate ϵ_r follows a lognormal distribution, with the variance σ_r^2 of $log(\epsilon_r)$ given by:

$$\sigma_r^2 = B + \pi\, log(L/r) \tag{23}$$

where, B is a constant associated to the macrostructure of the flux, π is a universal constant, and L the largest external scale. The probability density function over a range of scales r can be written as follows:

$$\Delta u = \epsilon_r^{1/3} r^{1/3} \tag{24}$$

This law is known as the Refined Similarity Hypothesis (RSH) of Kolmogorov. By considering $\zeta(3) = 1$ from the Eq. (24), the scaling exponent function is given by:

$$\zeta(q) = \frac{q}{3} - \frac{\pi}{18}(3q - q^2) \tag{25}$$

Schertzer & Lovejoy (1987) also proposed a model including the intermittency, where the scaling exponent function involves the scaling moment function $K(q)$:

$$\zeta(q) = qH - K(q) \tag{26}$$

The function $K(q)$ could be characterised by only three parameters in the Universal Multifractal framework.

3. Self-similarity extension: from fractal sets to multifractals

Based on the fractal geometry, Parisi & Frisch (1985) introduced the term "multifractal" to explain the nonlinearity of the scaling exponent function. They considered a turbulent field (e.g., the velocity field) u on a space S dimension d (Lovejoy & Schertzer, 2013). The points $u(r)$ of the velocity field have a singularity γ of order $h > 0$ at the point x if:

$$\lim_{r \to 0} \frac{u(x + r) - u(x)}{r^h} \neq 0 \tag{27}$$

This leads to say that:

$$\Delta u \approx r^{-h} \tag{28}$$

In this way, $S(h)$ is the set of points for which the field has a singularity of order h, called the "Hölder" exponent, or singularity strength. Hence $S(h) \subset S$, and the set $S(h)$ has a fractal dimension D_h. Thus, different singularities γ (defined as $\gamma = \log(\epsilon_\lambda) / \log(\lambda)$) are associated with fractal sets having different dimensions D_h, which leads to say that $u(r)$ is multi-fractal.

From the definition of fractal dimension and box-counting, D_h is nonnegative and its link with $c(\gamma)$ is found:

$$c(\gamma) = d - D_h \tag{29}$$

where, $c(\gamma)$ is the codimension function (Schertzer & Lovejoy, 1987) bounded by d. Hence, the events with low occurrence have a dimension of 0 and those with more frequency fill the space, the $0 \leq c(\gamma) \leq d$.

3.1 Statistical properties of multifractal fields

The statistical properties of a multifractal field ϵ_λ at a given resolution λ are defined by two scaling laws (Lovejoy & Schertzer, 2013; Schertzer & Lovejoy, 1987, 1991): the probability distribution of the energy flux density ϵ_λ and the statistical moments; involving the codimension function $c(\gamma)$ and the scaling moment function $K(q)$, respectively.

The measure of the probability that ϵ_λ is greater than a given scaling threshold (singularity) λ^γ, is described by the relation (Schertzer & Lovejoy, 1987):

$$P(\epsilon_\lambda \geq \lambda^\gamma) \approx \lambda^{-c(\gamma)} \tag{30}$$

Being ϵ_λ the renormalized intensity of the field at the scale-ratio λ (defined in Eq. **Error! Reference source not found.**) and $c(\gamma)$ the codimension function associated to a given singularity γ.

Via the Mellin transform, Schertzer & Lovejoy (1987) demonstrated the probability distribution of Eq.33 is equivalent to the statistical moments. Hence, the scaling moment function $K(q)$ was introduced, to characterize the multifractal field ϵ_λ:

$$\langle \epsilon_\lambda^q \rangle \approx \lambda^{K(q)} \tag{31}$$

where, q is the statistical moments order and $\langle \epsilon_\lambda^q \rangle$ is the q moment mean of the intensity at the scale ratio λ.

3.2 Legendre Transform

Parisi & Frisch (1985) demonstrated for deterministic multifractals, the statistical moments as well as the probability distribution of singularities, are equivalents through the involutive Legendre Transform between $c(\gamma)$ and $K(q)$:

$$K(q) = \max_\gamma \big(q\gamma - c(\gamma)\big) = q\gamma - c(\gamma)$$

$$c(\gamma) = \max_q (q\gamma - K(q)) = q\gamma - K(q) \tag{32}$$

$c(\gamma)$ and $K(q)$ functions are convex (see Figure) and differentiable, Eq.35 becomes:

$$K(q) = q\gamma - c(\gamma);\ q = c'(\gamma) = \frac{dc(\gamma)}{d\gamma}$$

$$c(\gamma) = q\gamma - K(q); \gamma = K'(q) = \frac{dK(q)}{dq} \tag{33}$$

These relations demonstrate every moment of order q is related to only one singularity γ. Because of the conservation of flux from one scale to another, implies for $q = 1$:

$$K(1) = 0 \ and\ C_1 = K'(1) \rightarrow\ C_1 = \gamma_1 = c(\gamma_1) \tag{34}$$

C_1 is the "co-dimension of the mean" and it represents a characterization of the variability near the mean.

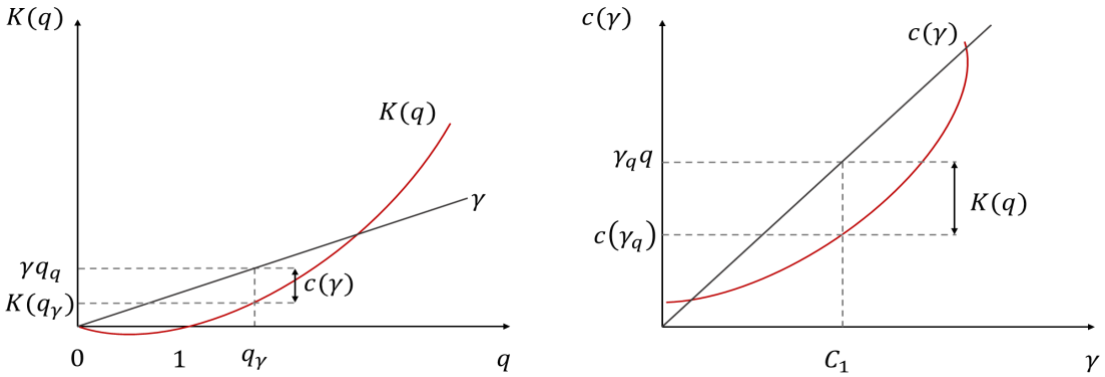

Figure 5. Legendre transform between $c(\gamma)$ and $K(q)$ functions. Adapted from Lovejoy & Schertzer (2013).

3.3 Universal Multifractals (UM)

As previously demonstrated, because of convexity of $c(\gamma)$ and $K(q)$, both functions depend on an infinity of parameters. Nevertheless, through a multiplicative central limit theorem, Schertzer & Lovejoy (1987) proposed the Universal Multifractal model, for which only few parameters are necessary to characterize $c(\gamma)$ and $K(q)$:

$$K(q) + Hq = \begin{cases} \frac{C_1}{\alpha - 1}(q^\alpha - q) & \alpha \neq 1 \\ C_1 q ln q & \alpha = 1 \end{cases} \quad (35)$$

$$c(\gamma) = \begin{cases} C_1 \left(\frac{\gamma + H}{C_1 \alpha'} + \frac{1}{\alpha}\right)^{\alpha'} & \alpha \neq 1 \\ C_1 \, exp\left(\frac{\gamma + H}{C_1} - 1\right) & \alpha = 1 \end{cases} \quad (36)$$

where α, C_1 and H are the three basic universal multifractal parameters:

- The mean singularity C_1, measure the clustering of the mean intensity (i.e., the fractality/sparseness of the mean field), and at the same time it corresponds to the codimension of the mean field:

  $$c(C_1 - H) = C_1 \quad (37)$$

  Note that for $C_1 = 0$ the field is homogeneous, and for greater values of C_1 the mean singularity of the field is sparseness.
- The Lévy index α, which indicates the extent of multifractality. This measures the mean intermittency evolve when considering singularity. The values of α varies between 0 and 2, being $\alpha = 0$ characteristic of monofractal fields, and $\alpha = 2$ characteristic of maximal occurrence of extremes (log-normal fields).

- The Hurst exponent H, that measure the degree of non-conservation of the mean field (for conservative field $H = 0$):

  $$\langle \epsilon_\lambda \rangle = \lambda^{-H} \quad (38)$$

After to prove the scaling behaviour of the field and to determinate the values of universal parameters, the Trace Moment (TM) and Double Trace Moment (DTM) techniques based on the function $K(q)$ are generally used.

3.4 Trace Moments (TM)

The Trace Moment technique allows to calculate the function $K(q)$ by means of the scale invariance moments of order q of the conservative field ϵ_λ (Schertzer & Lovejoy, 1987):

$$\langle \epsilon_\lambda^q \rangle \approx \lambda^{K(q)} \quad (39)$$

where, $\langle \epsilon_\lambda^q \rangle$ is the qth moment mean of the intensities at the scale λ and $\approx$ denotes the asymptotic equivalence. The function $K(q)$ is convex and it characterises the scaling invariance of the field (multifractal behaviour), showing the asymptotic behaviour of moment of order q.

To apply the TM method, the field must be considerate approximately uniform, and it is normalized assuming a mean of one, as follows:

$$\epsilon_\lambda = \frac{\epsilon_\lambda}{\langle \epsilon_\lambda \rangle} \quad (40)$$

The normalized temporal data series should be divided into non-overlapping intervals of a certain resolution λ. At each resolution λ, the sample is up-scaling independently and the

moment of order q is calculated ϵ_λ^q.The average moments of order q is calculated over all resolutions $\langle\epsilon_\lambda^q\rangle$, as follows:

$$\langle\epsilon_\lambda^q\rangle = \frac{\sum \epsilon_\lambda^q}{\lambda^D} \tag{41}$$

Then, the scaling behaviour of the field can be validated as a function λ, by plotting the logarithm of $\langle\epsilon_\lambda^q\rangle$ versus the logarithm of λ for different q values. The slopes of the linear regressions correspond to the estimations of $K(q)$, and the value of r^2 is used to validate the accuracy of the straight-line approximation. Then, the different $K(q)$ values and the associated q allows the estimation of the empirical $K(q)$ function.

Then, the UM parameters C_1 and α can be estimated using the $K(q)$ properties of the curve, by estimating the first two derivates of $K(q)$:

$$C_1 = K'(1)$$
$$\alpha = C_1/K''(1) \tag{42}$$

The appearance of the $K(q)$ function specifies the type of scaling involving: a straight line implies a monofractal structure whereas a convex curve implies a multifractal structure.

3.5 Double Trace Moments (DTM)

This technique is a direct method to obtain UM parameters, for a conservative multifractal field ϵ_λ. DTM generalise the TM technique based on a unique exponent q and the introduction of a second exponent η.

This method consists of performing a TM analysis to a renormalized η-power of ϵ_λ. For this purpose, firstly the field must be normalized, by arising the conservative field to the power η at the highest resolution, in the following way:

$$\epsilon_\lambda{}^{(\eta)} = \frac{\epsilon_\lambda{}^\eta}{\langle\epsilon_\lambda{}^\eta\rangle} \tag{43}$$

Then, the average statistical moments $\langle\epsilon_\lambda^{(\eta)q}\rangle$ also scales with the resolution λ:

$$\langle\epsilon_\lambda^{(\eta)q}\rangle \approx \lambda^{K(q,\eta)} \tag{44}$$

In this manner, the original field ϵ is transformed into ϵ^η and the function $K(q)$ into $K(q,\eta)$. Then, the qth-order moments of the renormalized field remain scale invariant:

$$\langle\epsilon_\lambda^{(\eta)q}\rangle \approx \lambda^{K(q,\eta)} \Rightarrow \left\langle\frac{\epsilon_\lambda{}^{\eta q}}{\langle\epsilon_\lambda{}^\eta\rangle^q}\right\rangle \approx \frac{\lambda^{K(q\eta)}}{\lambda^{qK(\eta)}} = \lambda^{K(q\eta)-qK(\eta)}$$
$$K(q,\eta) = K(q\eta) - qK(\eta) \tag{45}$$

when $\eta = 1$, $K(q,\eta)$ is reduced to $K(q)$. The expression above can be solved from the universality of $K(q)$ function:

$$K(q,\eta) = \eta^\alpha K(q) \tag{46}$$

With this expression, UM parameters can be directly estimated. In a log-log plot, $K(q,\eta)$ is plotted as a function of η, for a fixed value of q. The diagram allows to estimate α as the slope of the linear part of $K(q,\eta)$ and the intercept is used to determinate the parameter C_1.

A divergence of empirical functions of $K(q)$, deduced from the slope of $\langle\epsilon_\lambda^q\rangle$ and λ in logarithmic scale for different q values, and theoretical functions from the UM parameters with TM and DTM methods can occur. Then, after a given value of q the theoretical function of $K(q)$ becomes linear, leading to a departure from universal behaviour. This phenomenon is known as the multifractal phase transitions (Lavallée et al., 1991; Schertzer & Lovejoy, 1989), and it could be caused by the critical moment order of divergence q_D and the

undersampling q_s. According to Lavallée et al. (1991), in the case of one-dimensional field ($D = 1$) and the use one data sample $N_s = 1$, the value of q_s is given by the formula:

$$q_s = \left(\frac{D}{C_1}\right)^{1/\alpha} \tag{47}$$

The critical order of divergence of moments q_D represents q value for which the extreme values of the field are dominant. Thus, the average statistical moment or order $q \geq q_D$ tend to infinity.

4. Scaling invariance behaviour of the BGW's thermal fluxes

In order to explore the scaling behaviour of micrometeorological measures carried out over the Blue Green Wave, the power spectral density and the structure function will be investigated. As presented in Deliverable 1.1, some data collected from techniques of ET measure were not exploitable and because of frequency of measure and length of campaigns, the number of datapoints were limited (maximum 32 data points). However, as the application of statistical analysis requires sufficient data, a new campaign of measurements was performed with the LAS MKI and the CNR4 for a longer period. Due to irregularity of measure with the Ch and missing values of CWS665 sensors (which is not favourable to the application of the FFT), the Ch and WB were not analysed. Despite the main interest of this research concerns BGW's fluxes during summer months, particularly in UHI events, this long campaign with the LAS MKI scintillometer was conducted during the winter months of December 2019 and January 2020 because logistic convenience. Hence, this is considered a first approximation of the variability of thermal fluxes in the BGW.

4.1 Data set

The LAS MKI transmitter and receiver units were mounted over the roofs of the Carnot and Bienvenüe buildings, at the core of the Cité Descartes (See Figure 6). The CNR4 was located next to the LAS receiver, 1.5 m above the ground, to monitor radiation components and approximate the conditions of atmospheric stability. Finally, as optical LAS MKI is more sensitive to temperature fluctuations, the air temperature was monitored too.

Figure 6. Plan view of beam in winter months.

The elevations (including the height of buildings) are 119.15 m and 117 m for the transmitter and the receiver, respectively. Just like the summer set-up campaign, the effective beam

height was calculated through EVATION software from the elevation of units and the surface topography of the transect profile (see Figure 7).

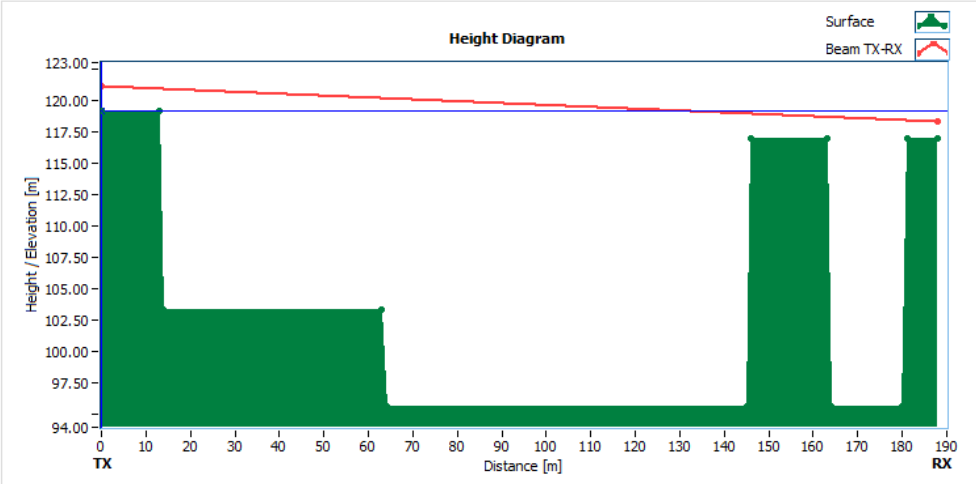

Figure 7. Horizontal path length and effective height of LAS during winter months.

The path length between both units was 190 m, hence diaphragms for short-range applications were necessary. The EM alignment pass over the BGW, stone floor and buildings roofs.

Table 1. LAS MKI Setting Experiment on winter months.

Feature	Value
D [cm]	10
R [m]	190
z_{LAS} [m]	11.679
z_0 [m]	0.5
d [m]	0
z_T [m]	2
z_R [m]	1.4
Duration	2019/12/18 - 2020/01/17

The sampling frequency was 1 Hz with 10 minutes average for the LAS and 5 minutes average for the CNR4. The output LAS signals were controlled via the QC parameter as explained in Deliverable 1.1. The measurements represented in the Figure 8 shows two periods of time where the values of $Demod$ and UCn_2 exceed -50 mV and 0 V respectively:

- 2020/01/01 03:00 to 2020/01/01 19:00
- 2020/01/16 02:00 to 2020/01/16 10:30

Without these disruptions, the values of UCn_2 ranges between -1.5 and -2V, while $Demod$ values do not go beyond -350 mV.

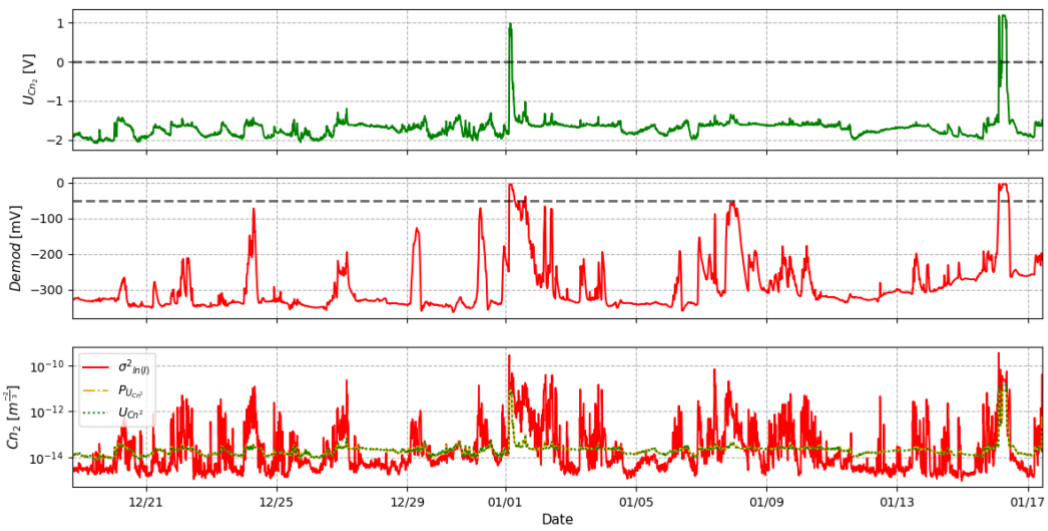

Figure 8. LAS MKI signals: $\overline{UCn_2}$(upper) and $\overline{Demod}$ (middle) and $\overline{C_n{}^2}$ calculations (bottom). The QC parameters are marked with the grey dotted line.

To understand potential causes of intensity reduction in LAS MKI measurements, the rainfall data were analysed in Figure 9. The rainfall intensity was collected every 5 minutes by three optical disdrometers of the Fresnel Platform from HM&Co Laboratory (see more details in Gires et al., 2018), located just next to the LAS MKI receiver unit on the roof of the Carnot building. A significant event of rainfall of 30 mm/h was recorded on December 27th, which caused slight alterations on the $\overline{Demod}$ signal, but that did not affect the QC parameter. The rest of the rainfall events were lightly or moderated without significant consequence on the scintillometer measure.

Regarding the atmospheric conditions during the campaign, most of the days in December were sunny and cloudy, while in January low rates of solar radiation $\overline{Sw}$ were more frequent. Daily fluctuations of temperature were large during cloudless days (12/29 to 01/01), ranging from 0 to 10 °C. However, there was no specific temperature variation having an impact on the LAS measurements. Hence, meteorological conditions can be discarded from LAS signal disruption.

The values of $\overline{Rn}$ were used to determinate the stability of the atmosphere since there are no measures of thermal gradient between the ground and the upper atmosphere. Thus, just like works of Han et al. (2019) and Kohsiek et al. (2006), measurements taken under conditions of $\overline{Rn}$ greater than 10 W/m² were considered as unstable atmosphere.

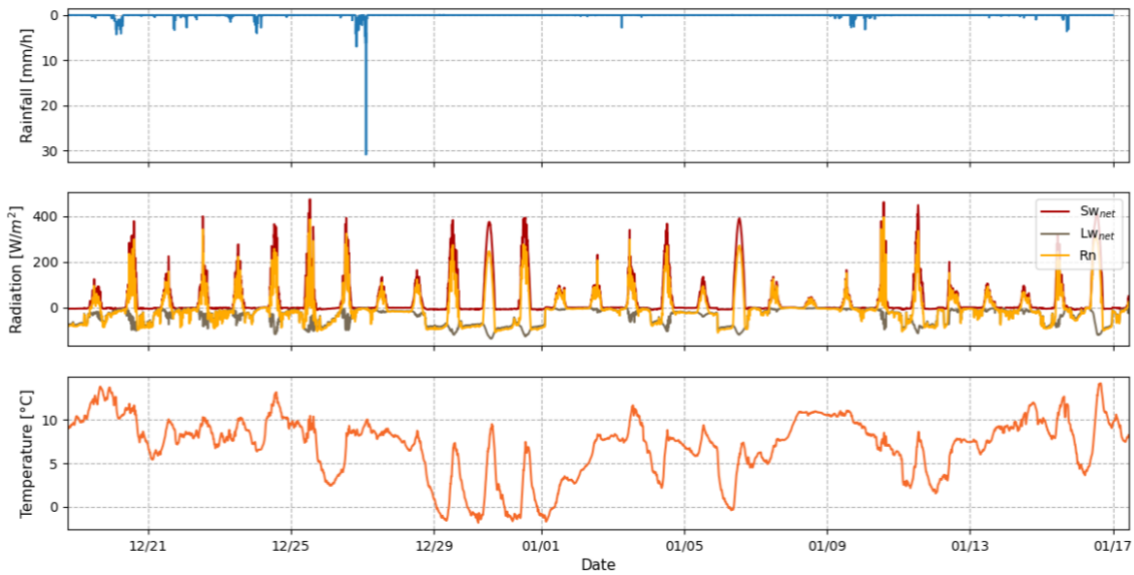

Figure 9. Meteorological conditions during winter months.

4.2 Spectral analysis

To avoid errors in the statistical analysis due to inaccuracy of SEB fluxes measures that may be transferred into Qe, as well uncertainty of parameters involved in the deduction of SEB parameters, the spectral analysis was applied to raw data of C_n^2 from LAS MKI, through the FFT algorithm.

The three methods to estimate C_n^2 from the output signals of LAS, discussed in Deliverale 1.1, can be appreciated at the bottom of Figure 9. There is a good fit between C_n^2 from UCn_2 (green) and $PUCn_2$ (yellow) ranging around 10^{-14} and 10^{-13}. Concerning C_n^2 from $\sigma^2 \ln(I)$ (red), there are more significant fluctuations producing lower (10^{-15}) or higher (10^{-12}) turbulence intensity compared to the other estimations of C_n^2. C_n^2 and UCn_2 was used in the analysis.

The original data sets of C_n^2 in Figure 8 was divided into two periods (displayed in Figure 10) to avoid the signal disruption of January 1st of 2020 and rainfall event on December 27th of 2019. Since the computation of FFT uses sample length power of 2, both series of C_n^2 are composed of 1024 data points, equivalent to 7 continuous days of measure.

A good linear scaling behaviour is observed for the first period in Figure 10.c. This scaling of C_n^2 ranges from log(f)=2.5 up to 5.5, corresponding to time-scale of 14 h and 41 min, respectively. The spectral slope is 1.649, comparable to the slope 5/3~1.66 in the inertial range of isotropic and homogeneous turbulence from K41. Regarding the second period in Figure 10.d, a similar behaviour is observed from log(f)=3 up to 5.5, corresponding to time-scale of 8.5 h and 41 min, slighted lower that the 5/3 of Kolmogorov.

The time scale of 8.5 h represented by the dotted vertical line is associated with the period of daylight time or solar forcing during a winter day. The radiation from the sun is fundamental, as it creates buoyancy heterogeneities and unstable atmospheric conditions when MOST theory is fully valid to deduce Qh. Regarding the 41 min, this is the time-scale of transition between unstable and stable atmosphere, this means the sunrise and sunset duration.

The spectral slopes of C_n^2 for both periods coincide with the assumption of Monin & Yaglom (1971) that power spectral density of turbulent fluctuations for a scalar follows the 5/3 law.

These results also agrees with the investigation of Maronga et al. (2013), where the power spectral density of the structure parameters of temperature $\overline{C_T{}^2}$ and humidity $\overline{C_Q{}^2}$ from Large Eddy Simulations in the convective boundary layer (where LAS is typically operated) followed a power law of 5/3 in the inertial range.

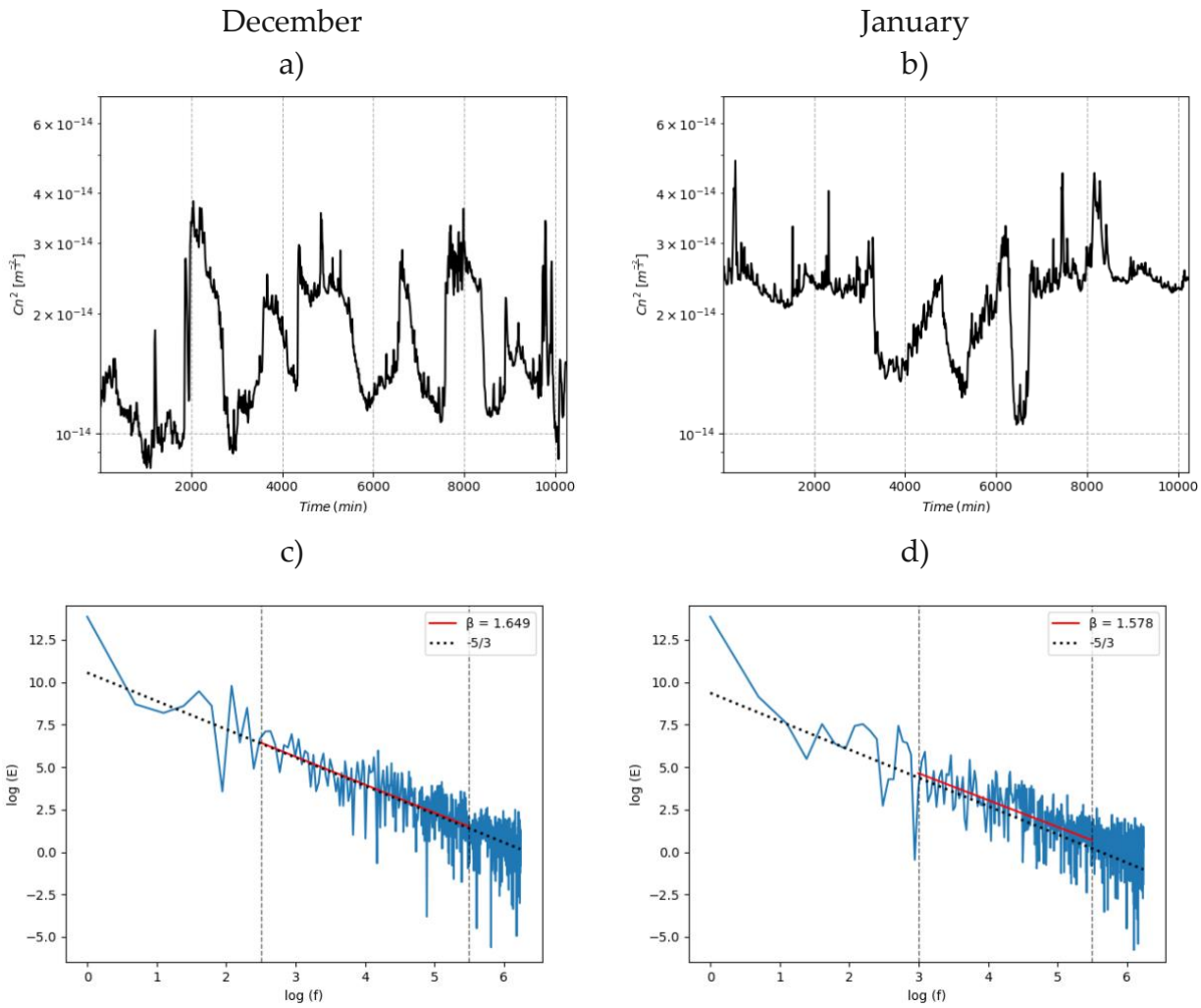

Figure 10. Two series of 10 minutes average of $\overline{C_n{}^2}$ in December and January and their respective power spectra density.

Since the fluctuations of the refractive index are caused by eddies with different temperature and humidity in the PBL, and the LAS's wavelength is mainly sensitive to temperature fluctuations, we will perform a spectral analysis of temperature measurements from the CNR4 (bottom of Figure 9). The same periods of analysis that $\overline{C_n{}^2}$ were considered and the size of the data sets was the double that $\overline{C_n{}^2}$ as the time period of measurement was 5 min, which corresponds to 2048 data points represented in Figure 11.

Time-scales related to solar forcing are marked in the energy spectrum of temperature: 24 h of diurnal cycle and 8.5 h of solar radiation. A single scaling range is observed after the 8.5 h up to 30 min (log (f)= 6.5). The spectral slope was 2.083 in December and 1.969 in January. This behaviour is associated with buoyancy effects and convective process in the atmosphere. In fact, these slopes are near to 11/5 scaling law predicted by Bolgiano-Oboukhov (BO) spectra, for a scaling stable stratified turbulence. Similar values of the spectral exponent were obtained by (Fitton, 2013; Karatasou & Santamouris, 2018) when analysing the scaling behaviour of air temperature and water temperature in a lake (Mezemate, 2014). The flattering of spectrum

of both series at highest frequencies (after 30 min), is related to white noise as the intensity of the spectrum is constant.

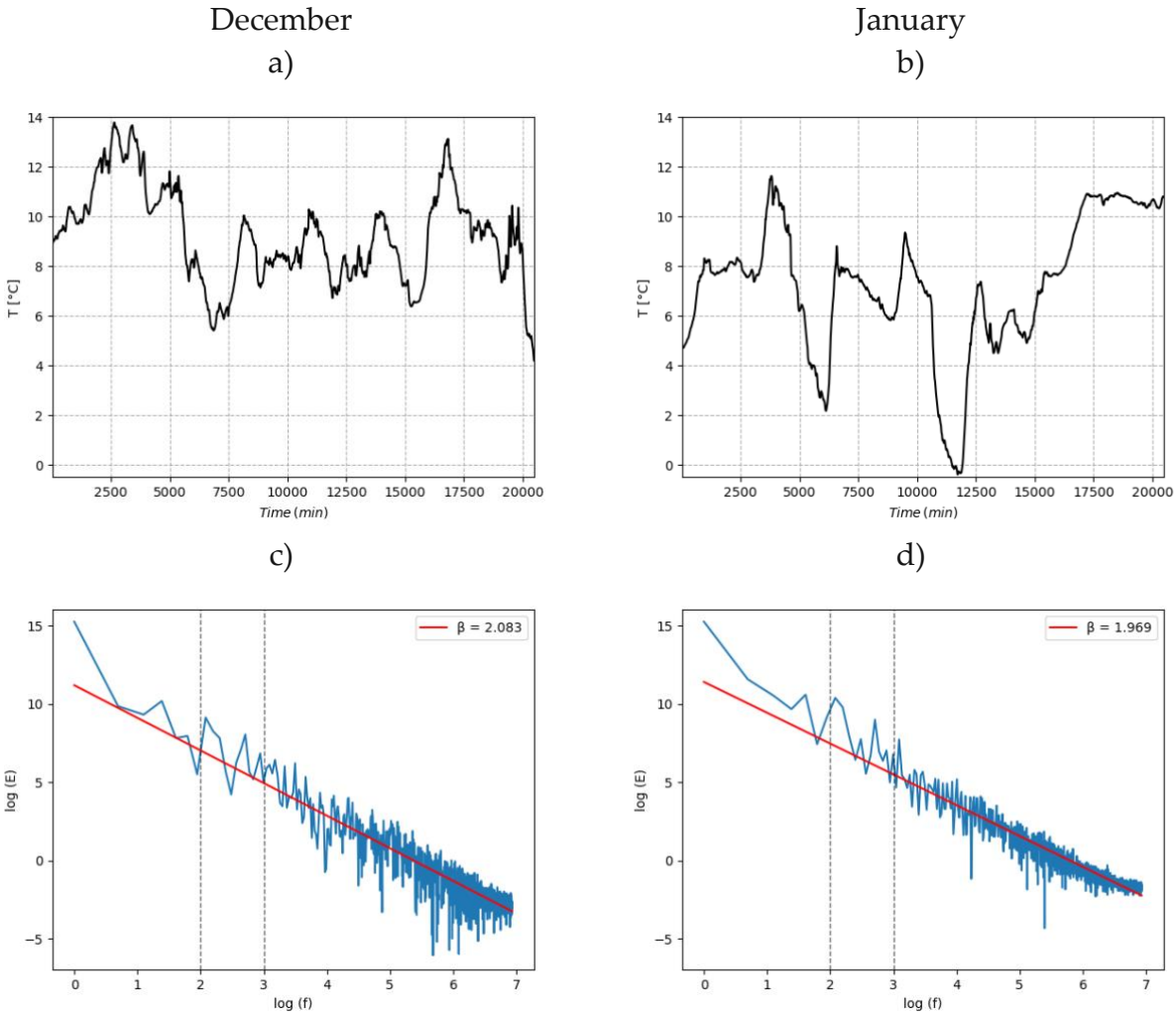

Figure 11. Two series of 5 minutes average of the air temperature in December and January and their respective power spectra density.

In conclusion, the scaling invariance of C_n^2 and temperature were verified through this spectral analysis. The spectral exponents are close to 5/3 for C_n^2 and 2 for the temperature, which indicates the fluxes is non-stationary ($\beta > 1$, the process is nonstationary). In addition, the spectral analysis proves to be a statistical tool of analysis to identify main frequencies influencing measurements, as well as potential sources of error. Nevertheless, the power spectral density only represents the second-order moment statistics, and its slope is not enough to fully describe the scaling behaviour of the data.

4.3 Structure function scaling exponent

The structure function introduced earlier allows to characterize the fluctuations of the flux, through the estimation of the scaling exponent function $\zeta(q)$ over several order moments q. As we are dealing with time series, the structure function is written for time series fluctuations as $S_a(\tau) = (\tau)^{\zeta(q)}$.

The structure function of C_n^2 was estimated over 1024 data points, for both periods of analysis, with $600s \leq \tau \leq 6.141 \times 10^5 s$ and the statistical order moments $q = [0.1{:}20]$ with increments of 0.1. Figure shows the results of the structure function obtained of December and January, for $q = 0.5, 1, 2, 2.5$ and 3. A single linear behaviour was observed in the range $600s$ up to $8.5h$. This confirms the scale invariance behaviour of C_n^2 for both periods of analysis observed previously with the power spectral density in the inertial range.

December January

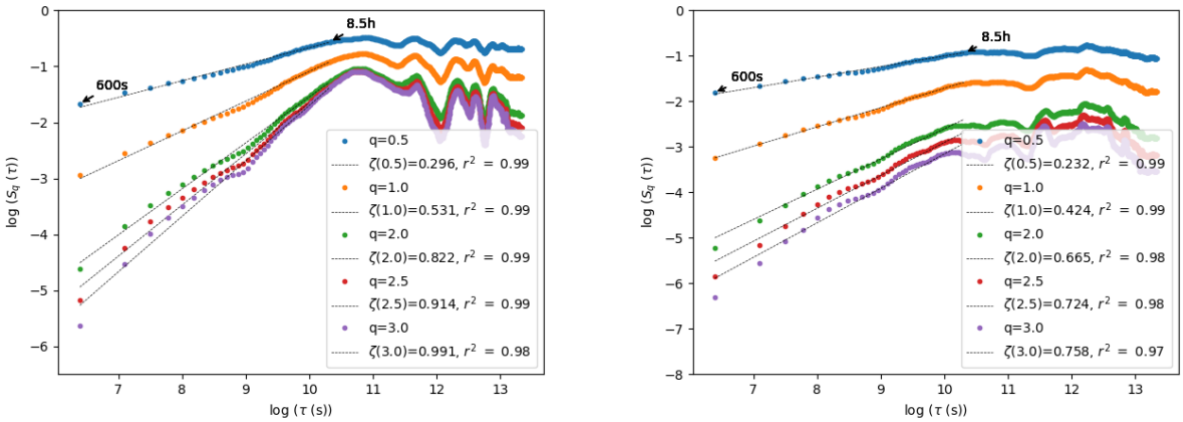

Figure 12. Structure function of C_n^2 increments in December and January.

The scaling exponent $\zeta(q)$ was estimated from the slopes of linear regressions in Figure 12 and was plotted in Figure 13. From the relations presented in Eq.24 and Eq.25, the estimates of H from $\zeta(q)$ and β were compared. The results presented in the Table 2 demonstrate the values of $H_{\zeta(1)}$ from $\zeta(q)$ were higher than those obtained from the spectral exponent H_β. The discrepancy between both methods is kept for the second-order moment in both periods. The average of H was predicted from the relation of the scaling exponent $\zeta(q)$ evaluated for all the moments q through Eq.24. For the period of December $H = 0.248 \pm 0.1$ and for January $H = 0.139 \pm 0.1$.

Table 2. $\zeta(q)$ estimates of C_n^2 following K41.

$\zeta(q) = qH$	December	January
$H_{\zeta(1)} = \zeta(1)$	0.51	0.424
$H_\beta = \beta - 1/2$	0.324	0.289
$\zeta(2)$	0.822	0.665
$\zeta(2)_\beta = \beta - 1$	0.649	0.578
H	0.248±0.1	0.139±0.1

The non-linearity and concavity of $\zeta(q)$ in Figure 13 is undisputed for both periods, indicating the multifractal nature of the structure parameter C_n^2. This agrees with the research of Pérez et al., (2014), which showed fractal dimension of surface patterns of a wavefront, measured through the box counting dimension, is not unique and it changed as convective turbulence is developed. Hence, fluctuations of C_n^2 from the BGW are not monofractal but multifractal.

December January

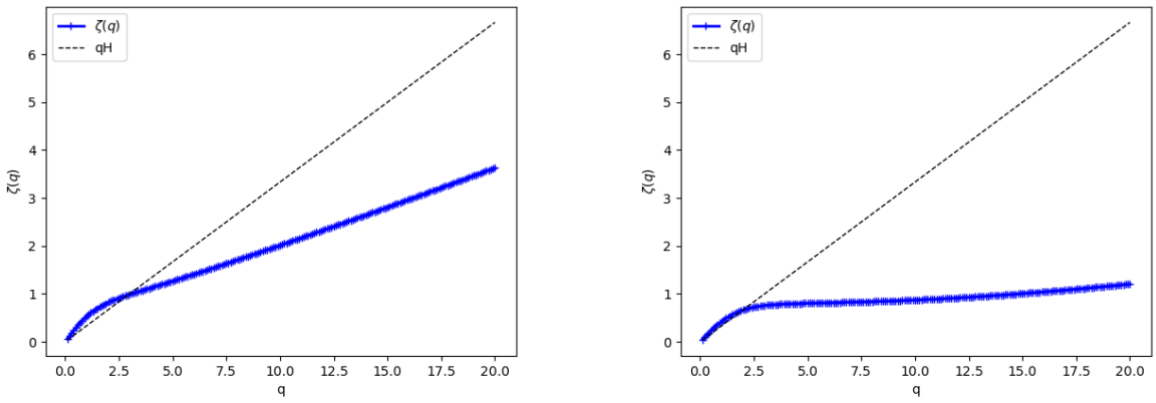

Figure 13. Scaling exponent $\zeta(q)$ of $C_n{}^2$ increments in December and January. The dotted line corresponds to the structure function with $H = 1/3$ for linear model of turbulence K41.

As $C_n{}^2$, the structure function of temperature series was evaluated, with 2048 data points, for the statistical order moments $q = [0.1:20]$ with increments of 0.1 and for each 300s interval, $300s \leq \tau \leq 6.141 \times 10^5 s$. Figure 14 plots the straight lines of the linear regression, which indicates the scale invariance is well respected over the range of time $300s$ up to $8.5h$. This behaviour is associated with buoyancy effects and convective processes in the atmosphere.

December January

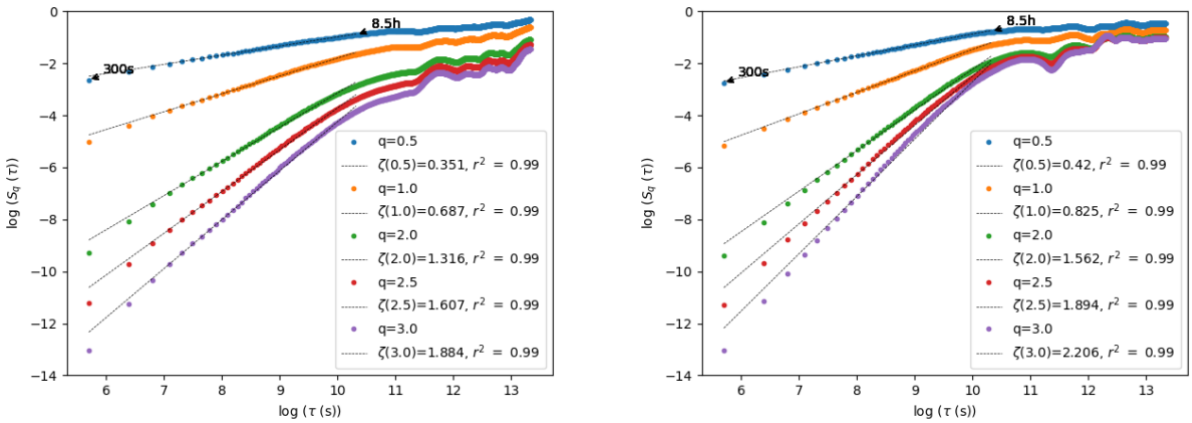

Figure 14. Structure function of temperature increments in December and January.

The empirical scaling exponent of the temperature for both periods of measure, estimated from the slopes in Figure 14, is shown in Figure . In comparison with the monofractal process from the classical BO theory of buoyancy-driven turbulence, it is demonstrated the deviation of $\zeta(q)$ and the intermittent character of the temperature. For December period, the estimates of H from the spectral exponent β ($H_\beta = \beta - 1/2$) and the first-order structure function $\zeta(1)$ ($H_{\zeta(1)} = \zeta(1)$) are 0.541 and 0.674 respectively. However, for the period of January there is a discrepancy of 0.3 between H_β and $H_{\zeta(1)}$.

December January

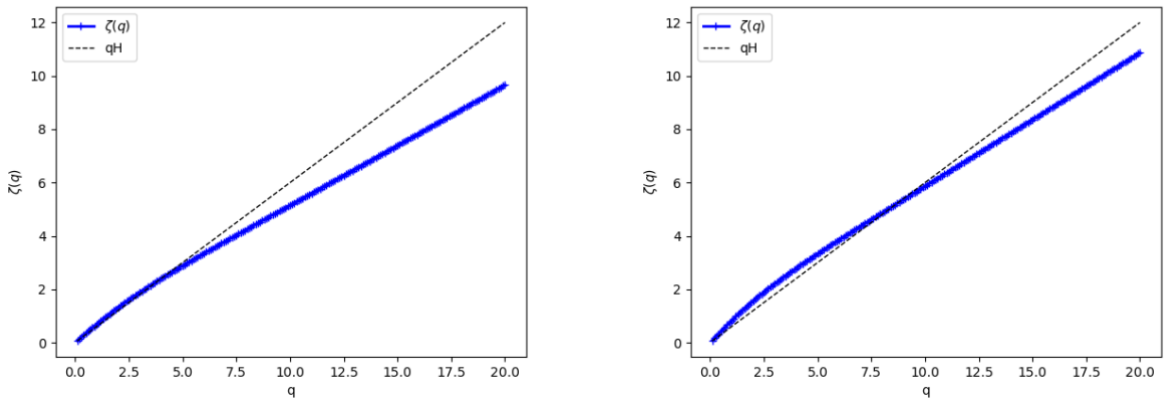

Figure 15. Scaling exponent $\zeta(q)$ of temperature increments in December and January. The dotted line corresponds to the structure function with $H = 3/5$ for BO theory.

From the results of the spectral density was proved the experimental data from the BGW are scaling and strongly non-conservative. The premised hypothesis the structure function follows a power law given by $\zeta(q) = qH$ and represents a (mono)-fractal behaviour, is not respected by ${C_n}^2$ and air temperature. This means a unique self-similarity law does not describe the fluctuations of ${C_n}^2$ and temperature because of intermittency, which is characterised by many fractal dimensions. Therefore, to fully characterize this non-linearity and scaling properties, the correction of intermittency given by $K(q)$ should be introduced, which will be characterised using the Universal Multifractal (UM) framework.

5. Characterisation of the scale invariance properties

The TM and the DTM technique are now applied to the experimental data from the BGW. The spectral slope of ${C_n}^2$ and temperature, in both periods of analysis, indicates fluctuations are non-conservative since $\beta > 1$. Therefore, the approach of Lavallée et al. (1993) from the absolute values of data increments was used to transform the non-conservative fields into conservative (which implies $H = 0$). This method was successfully applied by Stanic, (2020), to characterise UM parameters of spatial and temporal variability of the water balance components of the BGW: soil water content, rainfall intensity and drained discharge.

The statistical moments $\langle \epsilon_\lambda^q \rangle$ of ${C_n}^2$ fluctuations, were evaluated for different values of $q = [0.05, 3]$, for a series length of 1024 data points. Then, we processed to display at the top of Figure to check scaling. The fluctuations of ${C_n}^2$ shows a good scaling given by the value of r², mainly for the period of December. However, for $q = 0.1$ in both periods, the value of r² is the lowest.

The Figure b) and c) shows the average moments $\langle \epsilon_\lambda^{(\eta)q} \rangle$ as function of the resolution λ in logarithmic scale, with different values of η and $q = 1.5$. The accuracy of the linear regressions for any η is higher than 0.9 (rather better than TM), which demonstrates the scaling is well respected when λ varies from $\lambda = 1024$ up to $\lambda = 1$.

The slope of the linear regression $K(q, \eta)$ is obtained for every value of η and presented in Figure d) and e), from which α and C_1 parameters were deduced in the range of the η market with the red line. In December, universality is observed in the range $0.15 < \eta < 0.35$, while in January the range varies to $0.53 < \eta < 1.23$.

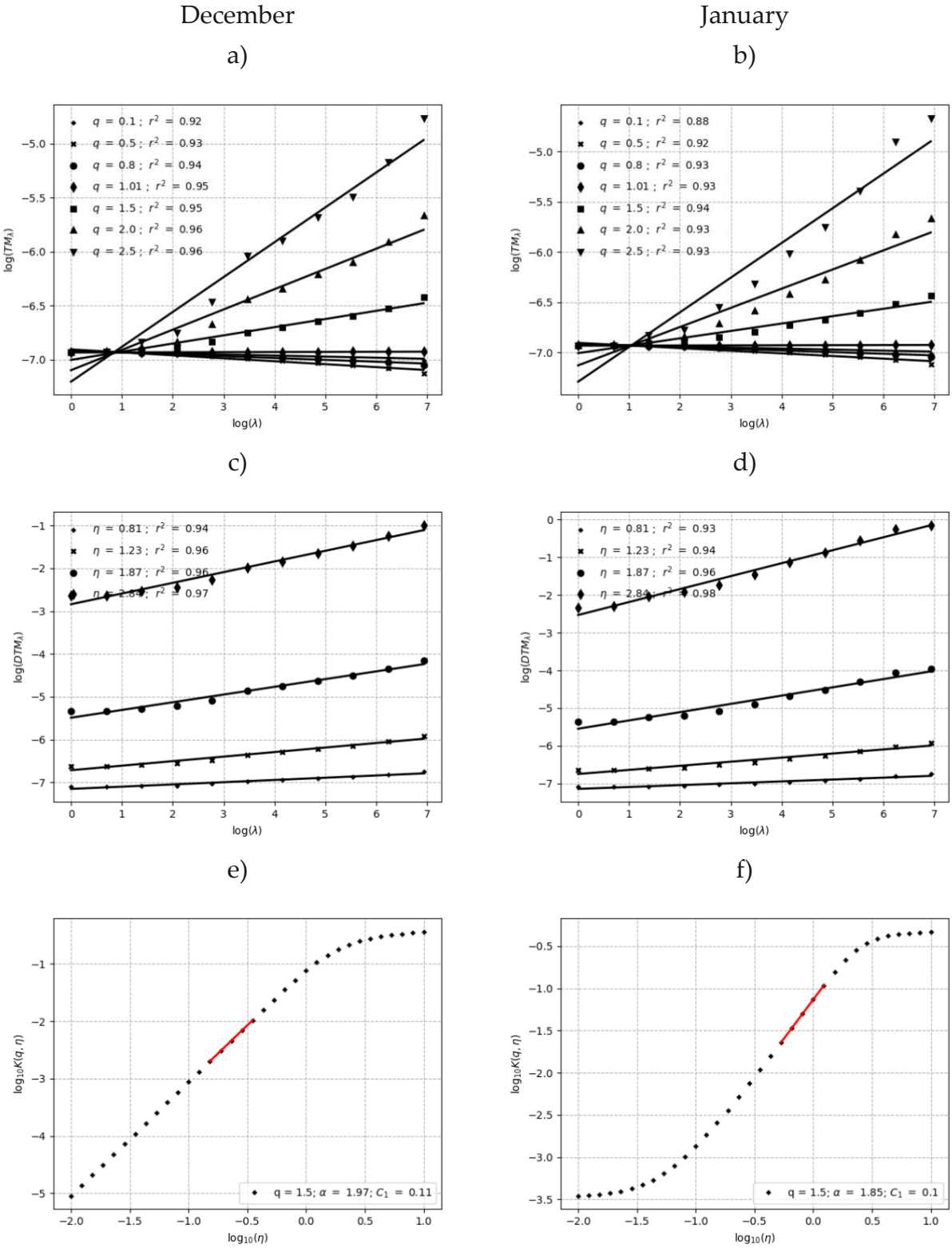

Figure 16. Characterisation of UM parameters to experimental C_n^2 data; a) and b) TM technique for different q values; c) and d) DTM technique with $\eta \in [0.01,10]$ and $q = 1.5$; e) and f) Statistical moment function $K(q,\eta)$ for different values of η, the red line represents the linear regression from which UM parameters are determined.

Table 3 presents the UM parameters (α and C_1) estimated through TM and DTM techniques. The values of α and C_1 are similar between both periods and techniques, which suggest the fluctuations have comparable features. The estimates of α in both periods, demonstrate strong multifractality of C_n^2 fluctuations, as α is nearly its maximum 2 (with both techniques). With regards to C_1, the estimates are not very large, which indicates mean intensity is not very sparse.

Table 3. UM parameters estimates of C_n^2.

Technique	**TM**		**DTM**	
Period	α	C_1	α	C_1
December/2019	1.839	0.106	1.97	0.11
January/2020	1.879	0.10	1.85	0.10

By estimating the linear regression over each q in Figure 16 a) and b), the empirical function of $K(q)$ can be deduced. As well, from UM parameter estimation the theoretical function of $K(q)$ is computed. The results in Figure 17 shows there is a good agreement between empirical and theoretical functions for q lower than 2.5 in December, and q lower than 3 in January, approximatively. This divergence was assessed though Eq. (50) from the UM parameters deduced with DTM method. Thus, q_s in December and January are 3.06 and 3.43 respectively, which is close to the values in Figure 17.

The characterisation of the intermittency of temperature fluctuations, implies following the same procedure applied previously for C_n^2. The estimates of TM and DTM over the whole range of scales, for December and January periods, are presented in Figure 18 and the UM parameters summarized in Table 4.

December January

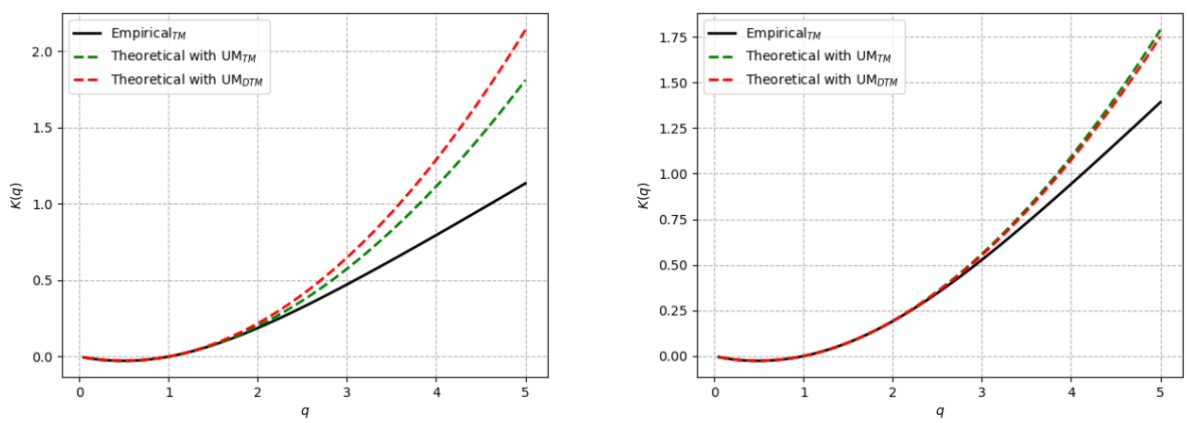

Figure 17. Comparison between curves of $K(q)$ of C_n^2, from the empirical value of the TM regression in Figure 16 a) and b), and from UM parameters and the Eq. (38).

Table 4. UM parameters estimates of temperature.

Technique	**TM**		**DTM**	
Period	α	C_1	α	C_1
December/2019	1.702	0.055	1.625	0.056
January/2020	1.680	0.073	1.587	0.075

In both techniques, the accuracy of the linear regression over all the scale-ratio λ at order $q = 0.1$ is not so good compared with higher values of q. However, the scale invariance

behaviour of temperature fluctuations is well observed over all the range of scales in the results of DTM. The curves of $K(q,\eta)$ as function of η in logarithmic scale, with $q = 1.5$ is presented in Figure 18 e) and f). The slope was evaluated in the range of η between 0.81 and 1.87 for December, and between 0.65 and 1.52 for January.

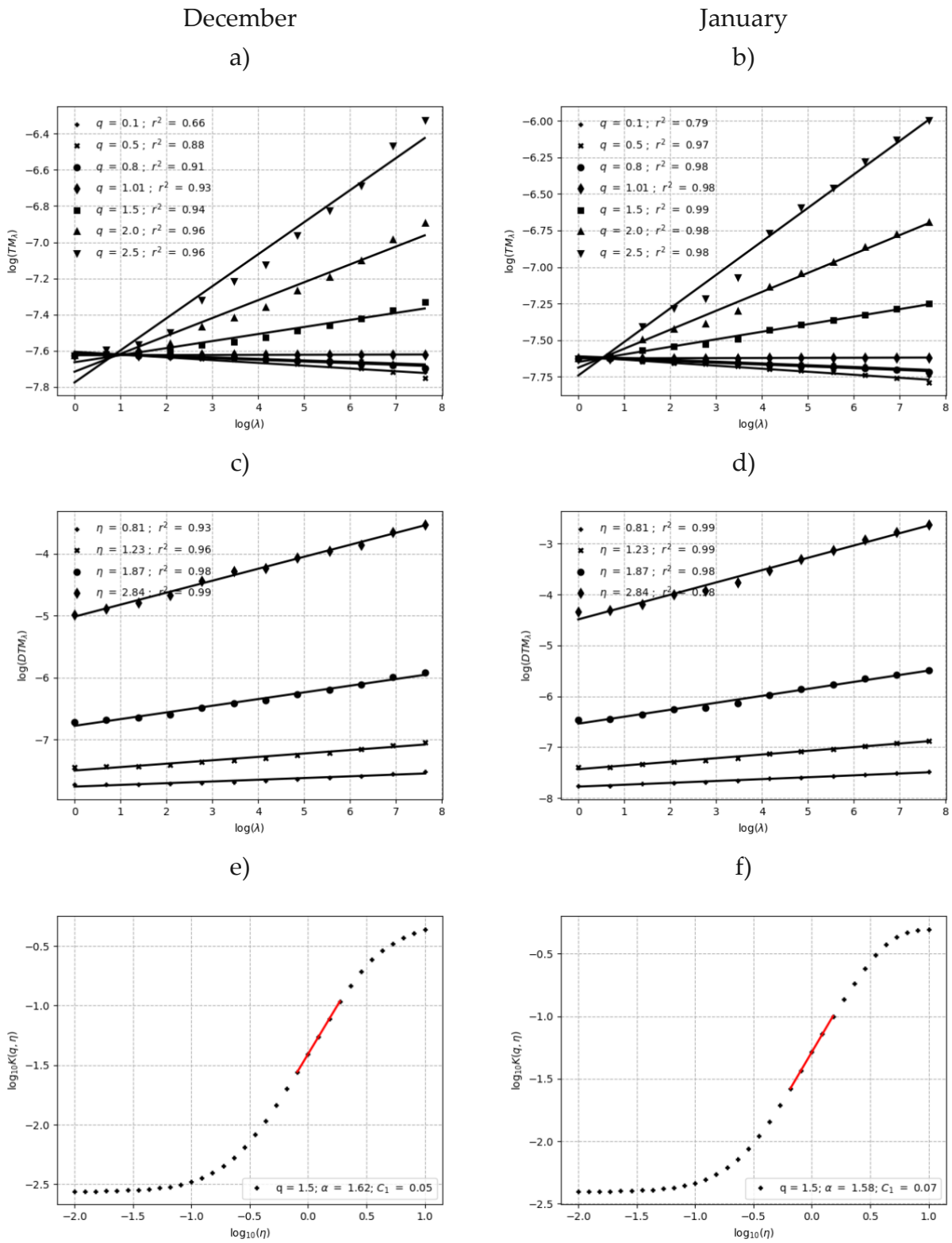

Figure 18. Characterisation of UM parameters to experimental temperature data; a) and b) TM technique for different q values; c) and d) DTM technique with $\eta \in [0.01,10]$ and $q = 1.5$; e)

and f) Statistical moment function $K(q,\eta)$ for different values of η, the red line represents the linear regression from which UM parameters are determined.

The values of α and C_1, are slightly different from those obtained of turbulent velocity measurements in the atmospheric boundary layer in Paris, α = 1.45 and C_1 = 0.29 (Schmitt et al., 1993). However, the estimates of C_1 are similar to the values found by Mezemate (2014) from water temperature data measured at different depths in the Creteil lake (Paris region). C_1 varies between 0.085 and 0.016, for the nearest depth to the surface of the lake (0.5m) and the deepest (4.5 m), respectively. In addition, the multifractal analysis conducted by Bodri & Cermak (2005) for two temperature series measured in boreholes in Kamchatka Peninsula (Russia), led to find similar values of C_1 (0.097 and 0.098) and lower values α (1.32 and 1.24) that in the BGW.

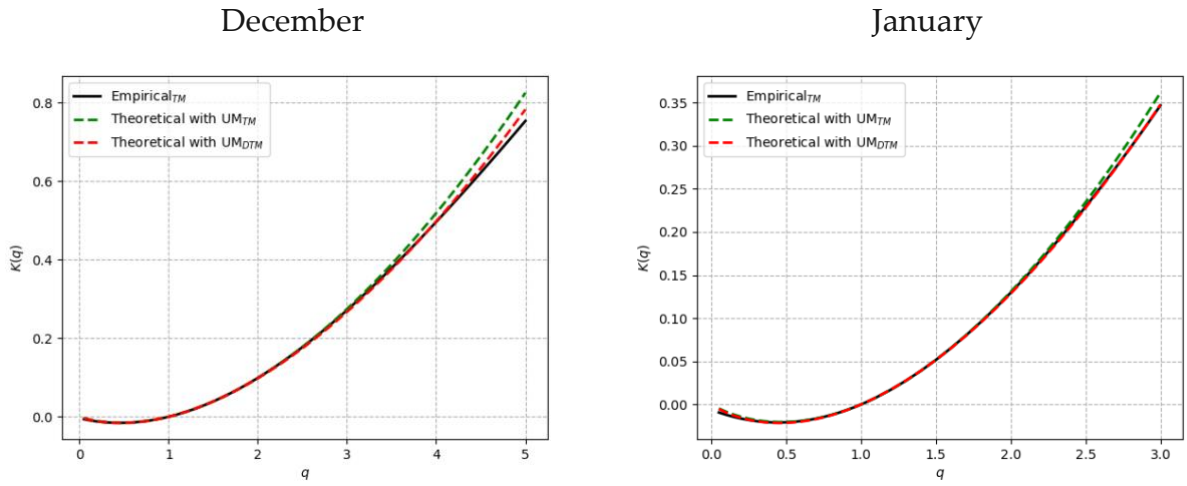

Figure 19. Comparison between curves of $K(q)$ of temperature, from the empirical value of the TM regression in Figure 16 a) and b), and from UM parameters and the Eq. (38).

The curves of $K(q)$ in Figure 19 are convex in both periods which proves the statistics of the temperature in the BGW are multifractals. In addition, $K(q)$ from TM and DTM have a good agreement with the empirical curve of $K(q$A slight deviation apparently occurs over $q = 4$ in December and $q = 3$ in January. According to estimation of q_s in December and January, the divergence occurs in q values of 5.86 and 5.10, respectively.

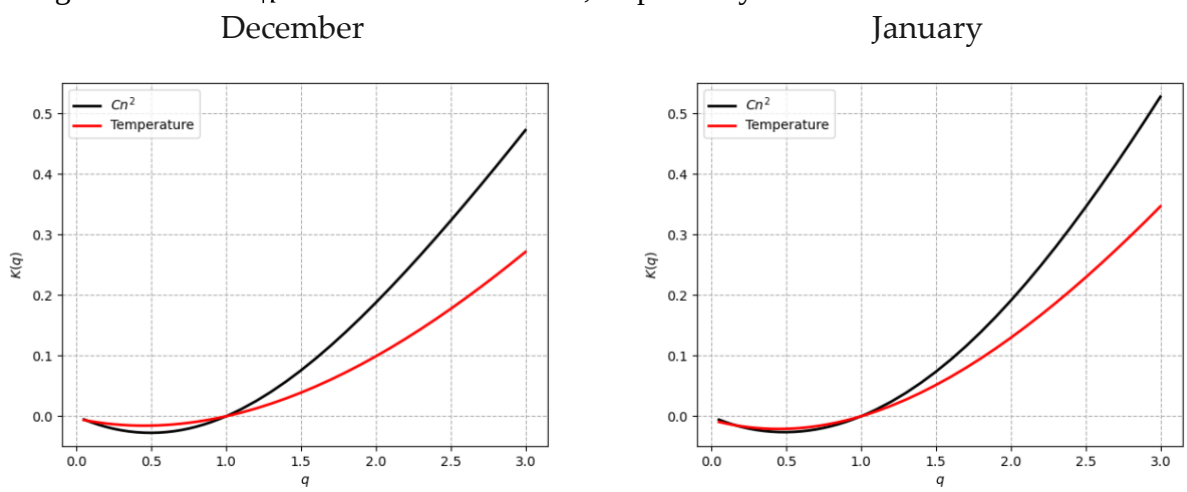

Figure 20. Empirical $K(q)$ functions of $C_n{}^2$ and temperature data measured in the BGW in December and January.

It appears reasonable to expect variability of C_n^2 is close to that of the temperature as LAS MKI is mainly sensitive to temperature fluctuations in the horizontal path-length between transmitter and receiver. The empirical functions $K(q)$ of C_n^2 and temperature in December and January, displayed in Figure 20, partially validate this assumption, as $K(q)$ of C_n^2 in both periods is much more convex than the temperature. This may suggest C_n^2 measurements are the results of turbulent processes additional to the heat convection, such as the advection from the surrounded atmosphere. Therefore, it may be useful some additional experimentation, that includes wind speed, to analyse the variability C_n^2 and temperature fluctuations.

Through the codimension function $c(\gamma)$, the fractal dimension value can be deduced. Figure 21.a shows the corresponding estimates of $c(\gamma)$ in the framework of the codimension multifractal formalism, using UM parameters and Eq.39. Then, the latter is related to the geometrical dimension multifractal formalism (Parisi & Frisch, 1985). In the dimension multifractal formalism, for each singularity a_D the function $f(a_D)$ is linked to the codimensions as $f(a_D) = D - c(\gamma)$, and $a_D = D - \gamma$. The subscript D of $f(a_D)$ and a_D represents the dimension D of the space on which the process is observed, thus $D = 1$ for temporal series.

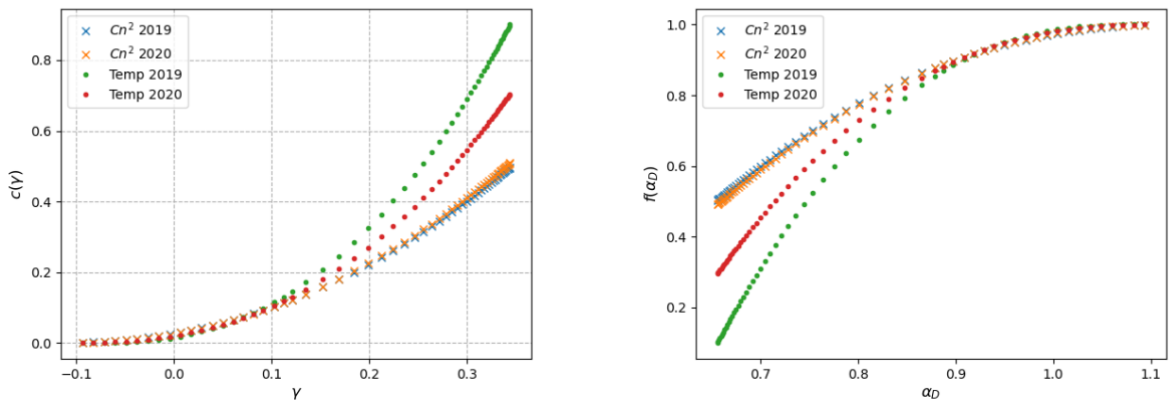

Figure 21. a) The codimension $c(\gamma)$ function of C_n^2 and temperature. b) Singularity spectrum, $f(a_D)$ as a function of singularities a_D.

The fractal dimension $f(a_D)$ was plotted as a function of the order of singularity a_D in Figure 21 for C_n^2 and temperature in December and January. This plot is known as the "singularity spectrum" or "multifractal spectrum". Thus, multifractality is corroborated since spectrums of both temporal series, C_n^2 and temperature, exhibit a distribution of singularities (Hölder exponents) and its corresponding fractal dimension.

The spectrums of all temporal series in both periods are asymmetrical between a_D range going from 0.6 up to 1.1. All spectrums are left-skewed as only large fluctuations ($q > 0$) are evaluated. The spectrum of C_n^2 in both periods has a quite similar multifractal behaviour, while that of the temperature is lower in December 2019 than in January 2020. Nevertheless, when $a_D = 1.1$ the spectrum of C_n^2 and temperature in both periods converges to the same $f(a_D)$ value, which not exceed the dimension of the observing space.

6. Conclusions and Perspectives

In this chapter statistical tools to address the scaling invariance of measurements of scintillometry and temperature over the BGW were used. The spectral analysis, as well as the scaling exponent of the parameter of refraction index of air C_n^2, demonstrated its scale invariance behaviour. The spectral analysis indicated a single scale-invariance in the time-scale of 14-8h to 41 min with a slope close to that of K41, 1.64 in December and 1.57 in

January. Regarding the temperature, a linear behaviour for the whole range of scales was observed and the spectral exponent is close to that of BO (2.09 and 1.97).

More precisely, the structure function that characterises the statistical properties of the fluctuations demonstrated a single scaling power law over 300s and 8.5h. In addition, the strong nonlinearity of the scaling exponent function $\zeta(q)$ shows that C_n^2 and temperature fluctuations are affected by intermittency and they are multifractal.

The UM parameters were characterised to consider the corrections of intermittency $K(q)$. The obtained values of Lévy index α and the mean codimension C_1 demonstrate, fluctuations of C_n^2($\alpha = 1.97 - 1.85$ and $C_1 = 0.11 - 0.10$ from DTM) and temperature ($\alpha = 1.625 - 1.587$ and $C_1 = 0.056 - 0.075$ from DTM) measured over the BGW in both periods of analysis, are multifractal and intermittent. The estimates of the UM parameters of the C_n^2 and temperature remain close to those obtained in the turbulent atmospheric layer.

The multifractal structure of C_n^2 and temperature increments was proved through the estimation of $K(q)$, which in both cases is convex and curved. In addition, the empirical function $K(q)$ of C_n^2 and temperature increments have some differences and diverge, indicating that although C_n^2 is mainly affected by temperature fluctuations, additional geophysical fields would impact heat convection in the surrounded atmosphere of the BGW.

Therefore, the temporal and spatial variability of thermal fluxes in the BGW requires a further analysis with more geophysical data, such as wind speed. This would allow to better characterise the scaling invariance as well as the statistical properties presented in this work.

Finally, through the codimension function $c(\gamma)$ and the UM parameters, the singularity spectrum of C_n^2 and temperature was characterised, to deduce the fractal dimension of their fluctuations that exceed different order of singularity.

7. References

Bodri, L., & Cermak, V. (2005). Multifractal analysis of temperature time series: Data from boreholes in kamchatka. *Fractals*, *13*(04), 299–310. https://doi.org/10.1142/S0218348X05002957

Calif, R., & Schmitt, F. G. (2014). Multiscaling and joint multiscaling description of the atmospheric wind speed and the aggregate power output from a wind farm. *Nonlinear Processes in Geophysics*, *21*(2), 379–392. https://doi.org/10.5194/npg-21-379-2014

Fitton, G. (2013). *Analyse multifractale et simulation des fluctuations de l'énergie éolienne* [These de doctorat, Paris Est]. http://www.theses.fr/2013PEST1110

Gires, A., Tchiguirinskaia, I., & Schertzer, D. (2018). Two months of disdrometer data in the Paris area. *Earth System Science Data*, *10*(2), 941. https://doi.org/10.5194/essd-10-941-2018

Han, P.-F., Wang, X.-S., & Wang, J.-Z. (2019). Using Large-Aperture Scintillometer to Estimate Lake-Water Evaporation and Heat Fluxes in the Badain Jaran Desert, China. *Water*, *11*(12), 2575. https://doi.org/10.3390/w11122575

Karatasou, S., & Santamouris, M. (2018). Multifractal Analysis of High-Frequency Temperature Time Series in the Urban Environment. *Climate*, *6*(2), 50. https://doi.org/10.3390/cli6020050

Kohsiek, W., Meijninger, W. M. L., Debruin, H. A. R., & Beyrich, F. (2006). Saturation of the Large Aperture Scintillometer. *Boundary-Layer Meteorology*, *121*(1), 111–126. https://doi.org/10.1007/s10546-005-9031-7

Kolmogorov, A. N. (1962). A refinement of previous hypotheses concerning the local structure of turbulence in a viscous incompressible fluid at high Reynolds number. *Journal of Fluid Mechanics*, *13*(1), 82–85.

Lavallée, D., Schertzer, D., & Lovejoy, S. (1991). *On the Determination of the Codimension Function*. https://doi.org/10.1007/978-94-009-2147-4_7

Lavallée, D., Lovejoy, S., Schertzer, D., & Ladoy, P. (1993). Nonlinear variability and landscape topography: Analysis and simulation. *Fractals in Geography*, 158–192.

Lovejoy, S., & Schertzer, D. (2013). *The Weather and Climate: Emergent Laws and Multifractal Cascades*. Cambridge University Press. https://doi.org/10.1017/CBO9781139093811

Mandelbrot, B. (1967). How Long Is the Coast of Britain? Statistical Self-Similarity and Fractional Dimension. *Science*, *156*(3775), 636–638. https://doi.org/10.1126/science.156.3775.636

Mandelbrot, B. (1982). *The Fractal Geometry of Nature*. W.H. Freeman and Company.

Maronga, B., Moene, A. F., van Dinther, D., Raasch, S., Bosveld, F. C., & Gioli, B. (2013). Derivation of Structure Parameters of Temperature and Humidity in the Convective Boundary Layer from Large-Eddy Simulations and Implications for the Interpretation of Scintillometer Observations. *Boundary-Layer Meteorology*, *148*(1), 1–30. https://doi.org/10.1007/s10546-013-9801-6

Mezemate, Y. (2014). *Analyse et modélisation multifractales des interactions ondes-turbulence-biologie dans un lac urbain* [These de doctorat, Paris Est]. http://www.theses.fr/2014PEST1166

Monin, A. S., & Yaglom, A. M. (1971). *Statistical Fluid Mechanics: Mechanics of Turbulence* (J. L. Lumley, Ed.; Vol. 1). MIT Press.

Obukhov, A. M. (1962). Some specific features of atmospheric turbulence. *Journal of Fluid Mechanics*, *13*(1), 77–81. https://doi.org/10.1017/S0022112062000506

Parisi, G., & Frisch, U. (1985). A multifractal model of intermittency. *Turbulence and Predictability in Geophisical Fluid Dynamics and Climate Dynamics*, 84–88.

Pérez, D. G., Barillé, R., Morille, Y., Zielińska, S., & Ortyl, E. (2014). Multifractal characteristics of optical turbulence measured through a single beam holographic process. *Optics Express*, *22*(16), 19538–19545. https://doi.org/10.1364/OE.22.019538

Schertzer, D., & Lovejoy, S. (1987). *Physical modeling and analysis of rain and clouds by anisotropic scaling multiplicative processes*. https://doi.org/10.1029/JD092ID08P09693

Schertzer, D., & Lovejoy, S. (Eds.). (1991). *Non-Linear Variability in Geophysics: Scaling and Fractals*. Springer Netherlands. https://doi.org/10.1007/978-94-009-2147-4

Schmitt, F., Schertzer, D., Lovejoy, S., & Brunet, Y. (1993). Estimation of universal for atmospheric turbulent multifractal indices velocity fields. *Fractals*, *01*(03), 568–575. https://doi.org/10.1142/S0218348X93000599

Stanic, F. (2020). *Suivi et modélisation à haute résolution des flux hydriques d'une toiture végétalisée* [These de doctorat, Paris Est]. http://www.theses.fr/2020PESC1012